

Article

# Optimization of Hole and Electron Transport Layer for Highly Efficient Lead-Free $\text{Cs}_2\text{TiBr}_6$ -Based Perovskite Solar Cell

Syed Abdul Moiz 

Device Simulation Lab, Department of Electrical Engineering, Umm Al-Qura University, Makkah 21955, Saudi Arabia; sasyed@uqu.edu.sa

**Abstract:** The methylammonium lead halide solar cell has attracted a great deal of attention due to its lightweight, low cost, and simple fabrication and processing. Despite these advantages, these cells are still far from commercialization because of their lead-based toxicity. Among lead-free perovskites, cesium-titanium (IV) bromide ( $\text{Cs}_2\text{TiBr}_6$ ) is considered one of the best alternatives, but it faces a lack of higher PCE (power conversion efficiency) due to the unavailability of the matched hole and electron transport layers. Therefore, in this study, the ideal hole and electron transport layer parameters for the  $\text{Cs}_2\text{TiBr}_6$ -based solar cell were determined and discussed based on a simulation through SCAPS-1D software. It was observed that the maximum PCE of 20.4% could be achieved by using the proper hole and electron transport layers with optimized parameters such as energy bandgap, electron affinity, doping density, and thickness. Unfortunately, no hole and electron transport material with the required electronic structure was found. Then, polymer NPB and  $\text{CeO}_x$  were selected as hole and electron transport layers, respectively, based on their closed electronic structure compared to the simulation results, and, hence, the maximum PCE was found as ~17.94% for the proposed  $\text{CeO}_x/\text{Cs}_2\text{TiBr}_6/\text{NPB}$  solar cell.

**Keywords:** perovskite; solar cell; lead-free perovskite;  $\text{Cs}_2\text{TiBr}_6$ ; SCAPS-1D; NPB;  $\text{CeO}_x$



**Citation:** Moiz, S.A. Optimization of Hole and Electron Transport Layer for Highly Efficient Lead-Free  $\text{Cs}_2\text{TiBr}_6$ -Based Perovskite Solar Cell. *Photonics* **2022**, *9*, 23. <https://doi.org/10.3390/photonics9010023>

Received: 26 November 2021

Accepted: 28 December 2021

Published: 31 December 2021

**Publisher's Note:** MDPI stays neutral with regard to jurisdictional claims in published maps and institutional affiliations.



**Copyright:** © 2021 by the author. Licensee MDPI, Basel, Switzerland. This article is an open access article distributed under the terms and conditions of the Creative Commons Attribution (CC BY) license (<https://creativecommons.org/licenses/by/4.0/>).

## 1. Introduction

It is unanimously accepted that the solar cell has the full potential to not only replace but also fulfill the enormous future demand for energy to sustain our existing commercial and industrial growth [1–3]. Currently, silicon solar cells are the most commercially available photovoltaic devices, but their cost is high compared to conventional energy resources. The requirement of cleanroom processing technology for Si is the main barrier to reducing their inherent cost for photovoltaic applications [4,5]. On the other hand, perovskite materials for solar cells have shown excellent performance at very low costs and their PCE has jumped from a few percent to >25% within a very short interval of time, and these materials can be processed even at room temperature [6].

Among these perovskites, the lead-based metal halide is an attractive perovskite with the highest reported PCE. However, at the same time, lead is a very toxic material as its presence in perovskite signifies a risk to human health, as well as green environmental life, which is a serious concern for their commercial applications [7]. Therefore, researchers are paying a lot of attention to proposing and investigating a lead-free perovskite for high-efficiency solar cells [8]. Among these materials, some lead-free perovskites such as the cesium titanium (IV) bromide ( $\text{Cs}_2\text{TiBr}_6$ ) compound has shown promising photovoltaic responses, but its PCE is still not comparable with methylammonium lead halide perovskite solar cells [9].

The direct-energy-bandgap perovskite compound  $\text{Cs}_2\text{TiBr}_6$  is a promising material that has very good optical, electrical, and photovoltaic properties and may replace methylammonium lead halide perovskite for next-generation photovoltaic applications [9–11]. On the other hand, robust titanium (Ti) makes  $\text{Cs}_2\text{TiBr}_6$  a tolerable and stable perovskite

semiconductor [12]. In this regard, the pioneering work was carried out by Chen and co-authors, and they investigated the photovoltaic response of the  $\text{Cs}_2\text{TiBr}_6$ -based solar cell, where  $\text{TiO}_2/\text{C}_{60}$  was used as an electron transport layer and  $\text{P}_3\text{HT}$  was used as a hole transport layer for PCEs up to 3.12% [9]. Table 1 summarizes some photovoltaic responses of the reported  $\text{Cs}_2\text{TiBr}_6$ -based solar cell with a given hole and electron transport layer. The data demonstrate that the  $\text{Cs}_2\text{TiBr}_6$ -based reported solar cells are still in the primitive stage and there is much room for further improvement of their photovoltaic responses.

**Table 1.** Summary of the published photovoltaic responses of  $\text{Cs}_2\text{TiBr}_6$ -based perovskite solar cell.

Year	Device	Study	HTL	ETL	Jsc	Voc	FF	PCE	Ref
2018	FTO/ $\text{TiO}_2$ / $\text{Cs}_2\text{TiBr}_6$ / $\text{P}_3\text{HT}$ /Au	Experimental	$\text{P}_3\text{HT}$	$\text{TiO}_2/\text{C}_{60}$	3.87	0.89	59.5	2.15	[9]
2018	FTO/ $\text{TiO}_2$ / $\text{C}_{60}$ / $\text{Cs}_2\text{TiBr}_6$ / $\text{P}_3\text{HT}$ /Au	Experimental	$\text{P}_3\text{HT}$	$\text{TiO}_2$	5.75	0.99	54.9	3.12	[9]
2019	CuSCN/ $\text{Cs}_2\text{TiBr}_6$ /CdS/Si	Simulation	CuSCN	CdS	8.9	–	–	6.68	[13]
2020	Glass/FTO/ $\text{TiO}_2$ / $\text{Cs}_2\text{TiBr}_6$ / $\text{Cu}_2\text{O}$ /A	Simulation	$\text{Cu}_2\text{O}$	$\text{TiO}_2$	25.82	1.1	51.7	14.68	[14]
2021	Ag/BCP/PCBM/ $\text{Cs}_2\text{TiBr}_6$ /NPB/ITO	Simulation	NPB	BCP/PCBM	16.66	1.29	78.1	16.85	[15]
2021	Au/PEDOT:PSS/ $\text{Cs}_2\text{TiBr}_6$ / $\text{TiO}_2$ /AZO	Simulation	PEDOT:PSS	$\text{TiO}_2$	18.2	1.38	71%	17.83	[16]

The active  $\text{Cs}_2\text{TiBr}_6$  as an absorber plays a vital role in absorbing the falling photons and converting them into electron-hole pairs as free carriers. These free carriers are extracted from the absorber and then transported through the electron transport layer (ETL) and hole transport layer (HTL) to reach their respective electrodes [15,17]. The most important criteria for the selection of the electron transport and hole transport layer depend on the electronic structure compatibility with the absorber layer. For effective hole as well as electron extraction, the valence-band/conduction-band offset ( $\Delta E$ ) between the absorber (e.g., perovskite) and hole/electron transport layer must be such that it also blocks the opposite electron/hole injection at the same interfaces [18]. The interactions of free carriers with interfaces as well as the respective transport materials are very complex and require comprehensive optimization for efficient solar cell applications [19–22]. The power conversion efficiency of  $\text{Cs}_2\text{TiBr}_6$ -based perovskite solar cells can further be improved by using the properly optimized parameters for both hole transport and electron transport layers, respectively. Now, a question arises about the ideal parameters for the best-suited electron and hole transport layer for the  $\text{Cs}_2\text{TiBr}_6$ -based solar cell. Once these ideal parameters are known, it will be helpful to select the most suitable from the available list of materials for both transport layers for highly efficient  $\text{Cs}_2\text{TiBr}_6$ -based perovskite solar cells. The important parameters that can easily be tuned for efficient photovoltaic response are listed as energy bandgap ( $E_g$ ), electron affinity (EA), electron and hole doping density ( $N_d$  and  $N_a$ ), and thickness of the hole and electron transport layer. Detailed information about the importance of these parameters for photovoltaic response can be found in the given references [22–25]. Simulating a solar cell through SCAPS-1D is one of the simple methods to estimate these tunable parameters. The simulation software approach is very quick and useful to determine the effects of thickness, doping density, temperature, spectral intensity, defects, and recombinational losses on the overall performance of a solar cell [24,26].

This study is also a part of our current work regarding the design of novel  $\text{Cs}_2\text{TiBr}_6$ -based lead-free perovskite solar cells [15,16]. Based on our previous results, as listed in Table 1, the ideal parameters of the hole transport layer and electron transport layer were estimated through SCAPS-1D software for highly efficient  $\text{Cs}_2\text{TiBr}_6$ -based perovskite solar cells. These parameters provide the framework for the selection of suitable hole and electron transport materials compatible with  $\text{Cs}_2\text{TiBr}_6$  for efficient lead-free perovskite solar cells.

## 2. Simulation Methodology and Material Parameters

### 2.1. Simulation Methodology

As stated earlier, SCAPS 1D (version 3.3.07) simulation software was used to determine the most suitable hole and electron transport parameters for the highly efficient Cs<sub>2</sub>TiBr<sub>6</sub>-based perovskite solar cell [16,26]. The SCAPS-1D is a one-dimensional simulation software that uses the combination of well-defined mathematical equations such as the Poisson equation (Equation (1)), electron continuity equation (Equation (2)), hole continuity equation (Equation (3)), total charge transport equation (Equation (4)), total charge transport equation for the electron (Equation (5)), total charge transport equation for the hole (Equation (6)), and optical absorption coefficient equation (Equation (7)) to define the photovoltaic response of a solar cell. Detailed information about these equations can be found elsewhere [16,23–26]. The model equations are

$$\frac{d^2\phi(x)}{dx^2} = \frac{q}{\epsilon_0\epsilon_r} (p(x) - n(x) + N_D - N_A + -0.3\rho_p - -0.3\rho_n) \quad (1)$$

$$\frac{dJ_n}{dx} = G - R \quad (2)$$

$$\frac{dJ_p}{dx} = G - R \quad (3)$$

$$J = J_n + J_p \quad (4)$$

$$J_n = D_n \frac{dn}{dx} + \mu_n n \frac{d\phi}{dx} \quad (5)$$

$$J_p = D_p \frac{dp}{dx} + \mu_p p \frac{d\phi}{dx} \quad (6)$$

$$\alpha(\lambda) = \left( A + \frac{B}{hv} \right) \sqrt{hv - E_g} \quad (7)$$

where  $\phi(x)$  is the electrostatic potential,  $q$  is the electrical charge with a typical value of  $1.602 \times 10^{-19}$  C,  $\epsilon_0$  and  $\epsilon_r$  are the absolute permittivity of vacuum and relative permittivity of a semiconductor, respectively,  $-0.3\rho_p$  is the hole defect density,  $-0.3\rho_n$  is the electron defect density,  $N_A$  is the shallow acceptor doping density,  $N_D$  is the shallow donor doping density,  $p(x)$  is the hole carrier density as a function of a thickness ( $x$ ),  $n(x)$  is the electron carrier density as a function of a thickness ( $x$ ),  $G$  is the carrier generation rate of free carriers,  $R$  is the total carrier recombination rate,  $J_p$  is the hole current density,  $J_n$  is the electron current density,  $J$  is the total current density,  $D_p$  is the free hole diffusion coefficient,  $D_n$  is the free electron diffusion coefficient,  $\mu_p$  is the free hole carrier mobility, and  $\mu_n$  is the free electron carrier mobility. Finally,  $\alpha(\lambda)$ ,  $h$ ,  $\nu$ ,  $E_g$ ,  $A$ , and  $B$  are the absorption coefficient as a function of wavelength, plank constant, optical frequency, energy bandgap, and arbitrary constant, respectively. All the simulations were carried out at the temperature of 300 K with the AM.1.5 standard illumination condition.

### 2.2. Device Structure

Generally, there are two device structures for perovskite solar cells reported such as a (a) mesoporous and (b) planar photovoltaic device structure. The planar device structure can further be classified into two groups, either a standard (noninverted) n-i-p or inverted p-i-n device structure [27]. A planar and noninverted n-i-p device structure was used for this study. As we are mainly interested in determining both hole and electron transport layer parameters for efficient Cs<sub>2</sub>TiBr<sub>6</sub>-based perovskite solar cells, the cell structure used in this study was kept very simple (ETL/Cs<sub>2</sub>TiBr<sub>6</sub>/HTL), as shown in Figure 1.

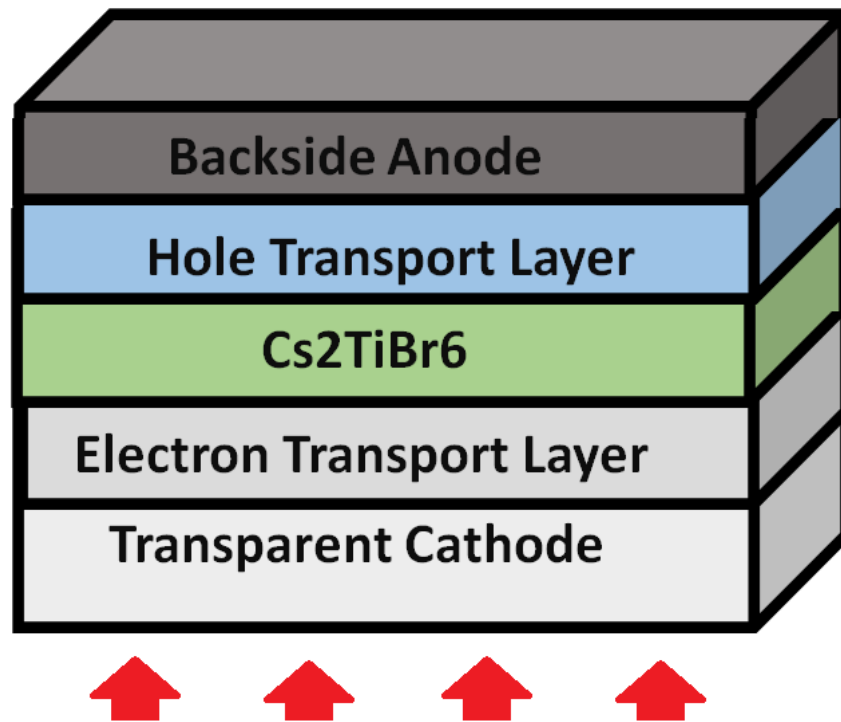


**Figure 1.** Schematic cross-section of perovskite solar cell, where absorber ( $\text{Cs}_2\text{TiBr}_6$ ) is sandwiched between hole transport layer (HTL) and an electron transport layer (ETL).

2.3. Simulation Flow Chart

Figure 2 demonstrates a flow chart used in this study to estimate the ideal HTL and ETL properties for  $\text{Cs}_2\text{TiBr}_6$ -based perovskite solar cells. The simulation is divided into five phases. In the first phase, EA is optimized for the HTL and then the ETL, followed by  $E_g$  optimization for each transport layer in the second phase. In the third and fourth phases, the doping density and thickness are optimized for each HTL and ETL, respectively. Meanwhile, in the final phase, the most suitable HTL and ETL materials are selected from Tables 2 and 3 based on the simulation output, and their photovoltaic responses are compared with the ideal ETL/ $\text{Cs}_2\text{TiBr}_6$ /HTL perovskite solar cell.

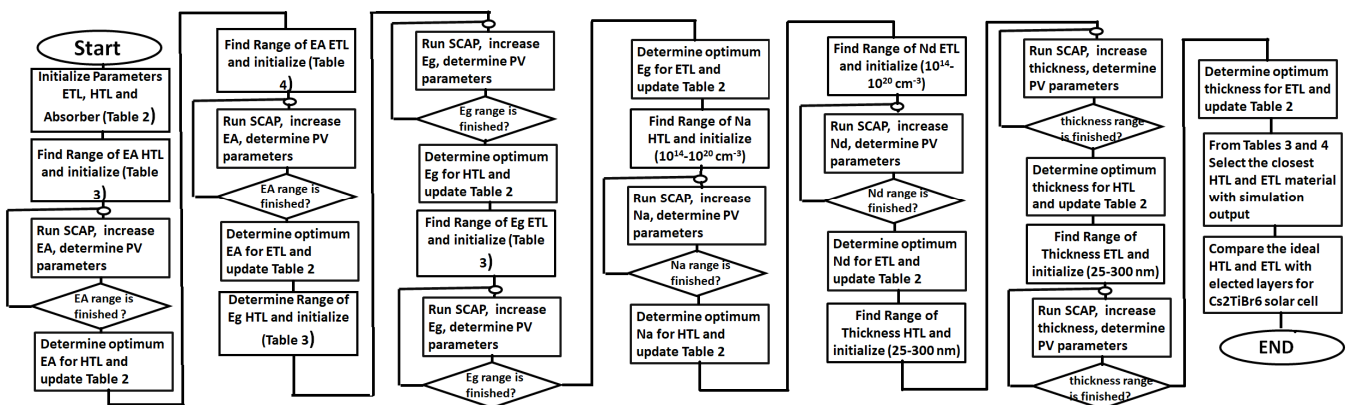


**Figure 2.** Flowchart used in this study to estimate the ideal hole transport layer (HTL) and electron transport layer (ETL) properties for  $\text{Cs}_2\text{TiBr}_6$ -based perovskite solar cell.

**Table 2.** Energy bandgap and electron affinity for commonly reported hole transport layer materials.

Transport Layer Material	Energy Band Gap (Eg, eV)	Electron Affinity (EA, eV)	Reference
Cu <sub>2</sub> O	2.17	3.2	[13]
Spiro-OMeTAD	3.2	2.1	[28]
PEDOT:PSS	1.6	3.5	[16]
NPB	3	2.4	[15]
P <sub>3</sub> HT	1.85	3.1	[29]
CuSCN	3.4	1.9	[29]
NiO	3.6	1.46	[28]
CZTS	1.5	4.5	[30]
CuI	2.98	2.1	[29,31]
CuO	1.3	4	[32]
MoO <sub>3</sub>	3	2.5	[29]
NiO	3.8	1.46	[29]
CuSbS <sub>2</sub>	1.58	4.2	[33]

**Table 3.** Energy bandgap and electron affinity for commonly reported electron transport layer materials.

Transport Layer Material	Energy Band Gap (Eg, eV)	Electron Affinity (EA, eV)	Reference
TiO <sub>2</sub>	3.26	4.26	[13,16]
ZnO:Al	3.3	4.6	[16,30]
IGZO	3.05	4.16	[29]
ZnO	3.2	4.26	[34]
SnO <sub>2</sub>	3.5	4	[35]
In <sub>2</sub> S <sub>3</sub>	2.8	4.7	[30]
CeOx	3.5	4	[28]
PCBM	1.9	3.9	[15]
BCP	3.5	3.7	[15]
CdS	2.4	1.8	[31]

Eg: min: 1.9, max: 3.5, median: 3.23.

#### 2.4. Physical Parameters

The physical parameters for the Cs<sub>2</sub>TiBr<sub>6</sub> as an absorber layer used in this simulation were selected from published results, which are listed in Table 4, while for the hole and electron transport layer, we classified their physical parameters as tunable and standard parameters. For tunable, we used a random value (randomly selected within a practical range) for just initialization in the first stage, and in the later stage, these parameters were updated according to the converged results in each simulation phase. These tunable parameters were energy bandgap, electron affinity, electron and hole doping density ( $N_d$  and  $N_a$ , respectively), and thickness of the hole and electron transport layer, while the standard parameters for the hole and electron transport layer were reasonably estimated (median reported values were selected) according to the well-reported published results. Similarly, the bulk density of defect tolerance ( $10^{15} \text{ cm}^{-3}$ ) was introduced in the absorber layer, as well as the hole and electron transport layer, as shown in Table 4.

**Table 4.** Physical parameters of Cs<sub>2</sub>TiBr<sub>6</sub> and hole and electron transport layer used in the simulation.

Physical Parameters	Symbol	Unit	HTL	Cs <sub>2</sub> TiBr <sub>6</sub>	ETL
Thickness	Th	nm	250	200	250
Energy Band Gap	E <sub>g</sub>	eV	2	1.8	2
Electron Affinity	χ	eV	4.5	4.47	4
Dielectric Permittivity (Relative)	ε	-	10	10	10
Effective Density of States at Valence Band	N <sub>V</sub>	cm <sup>-3</sup>	1 × 10 <sup>20</sup>	6 × 10 <sup>19</sup>	1 × 10 <sup>19</sup>
Effective Density of States at Conduction Band	N <sub>C</sub>	cm <sup>-3</sup>	1 × 10 <sup>20</sup>	2 × 10 <sup>19</sup>	1 × 10 <sup>19</sup>
Hole Thermal Velocity	V <sub>e</sub>	cm/s	1 × 10 <sup>7</sup>	1 × 10 <sup>7</sup>	1 × 10 <sup>7</sup>
electron Thermal Velocity	V <sub>h</sub>	cm/s	1 × 10 <sup>7</sup>	1 × 10 <sup>7</sup>	1 × 10 <sup>7</sup>
Electron Mobility	μ <sub>e</sub>	cm <sup>2</sup> /V.s	0.01	4.4	1
Hole Mobility	μ <sub>h</sub>	cm <sup>2</sup> /V.s	0.1	2.5	0.1
Uniform Shallow Donor Doping	N <sub>d</sub>	cm <sup>-3</sup>	0	1 × 10 <sup>19</sup>	1 × 10 <sup>18</sup>
Uniform Shallow Acceptor Doping	N <sub>a</sub>	cm <sup>-3</sup>	1 × 10 <sup>18</sup>	1 × 10 <sup>19</sup>	0
Defect Density	N <sub>t</sub>	cm <sup>-3</sup>	1 × 10 <sup>15</sup>	1 × 10 <sup>15</sup>	1 × 10 <sup>15</sup>
References			Random	[9,10,13]	Random

### 3. Results

#### 3.1. Optimization of Electron Affinity for Hole and Electron Transport Layer

In the first phase of the simulation, the optimized value of electron affinity for the hole transport layer was determined from the simulation and then updated in the physical parameters list of SCAPS 1D for further simulations. The electron affinity is directly related to the lowest unoccupied molecular orbital (LUMO) of the hole/electron transport layer and can be defined as the amount of energy (expressed in eV) needed to raise the free electron from the lowermost of the LUMO (or conduction band for conventional semiconductor) to the vacuum level. The matched electron affinity with its suitable energy bandgap leads to the efficient highest-occupied molecular orbital (HOMO) level, which, in turn, improves the hole/electron injection/blocking from the perovskite to the hole/electron transport layer [36,37]. However, before starting the simulation, it is important to determine the numerical range of electron affinity values from the reported hole transport layer for practical purposes; otherwise, nonrealistic physical parameters can be obtained from the output of the simulation results. Tables 2 and 3 show the relevant electronic parameters (energy bandgap and electron affinity) for the most reported hole transport layer and electron transport layer, respectively.

It is observed from the table that the maximum electron affinity is 4.7 eV, and the minimum electron affinity is 1.46 for the hole/electron transport layer. Thus, the maximum practical range of electron affinity for the simulation lies from 1.0 to 5 eV for both transport layers. We calculated the photovoltaic parameters by varying the electron affinity from 1.0 to 5 eV and determining the most optimum electron affinity of the hole/electron transport layer for the Cs<sub>2</sub>TiBr<sub>6</sub>-based solar cell, and the results such as open-circuit voltage, short-circuit current, fill factor, and power conversion efficiency are shown in Figure 3a,b, respectively. The figure demonstrates that the photovoltaic parameters such as open-circuit voltage, short-circuit current, and fill factor lead to the maximum PCE (~8.0%) of the cell at 3.0 eV of the electron affinity of the hole transport layer. Then, the new electron affinity value of the hole transport layer is updated in the software and the electron affinity of the electron transport layer for the given range (1 to 5 eV) is then estimated from photovoltaic parameters such as open-circuit voltage, short-circuit current, fill factor, and power conversion efficiency, as shown in Figure 3c,d. It is also observed from the figure that the electron affinity of the electron transport layer improves the open-circuit voltage, short-circuit current, fill factor, and hence, PCE (~11.1%) up to 4.6 eV of electron affinity and then starts to decrease. Thus, the SCAPS-1D parameters were updated with the optimized value of electron affinity at approximately 3 and 4.6 eV of the hole and electron transport layer, respectively, which improved the photovoltaic response for Cs<sub>2</sub>TiBr<sub>6</sub>-based solar cells.

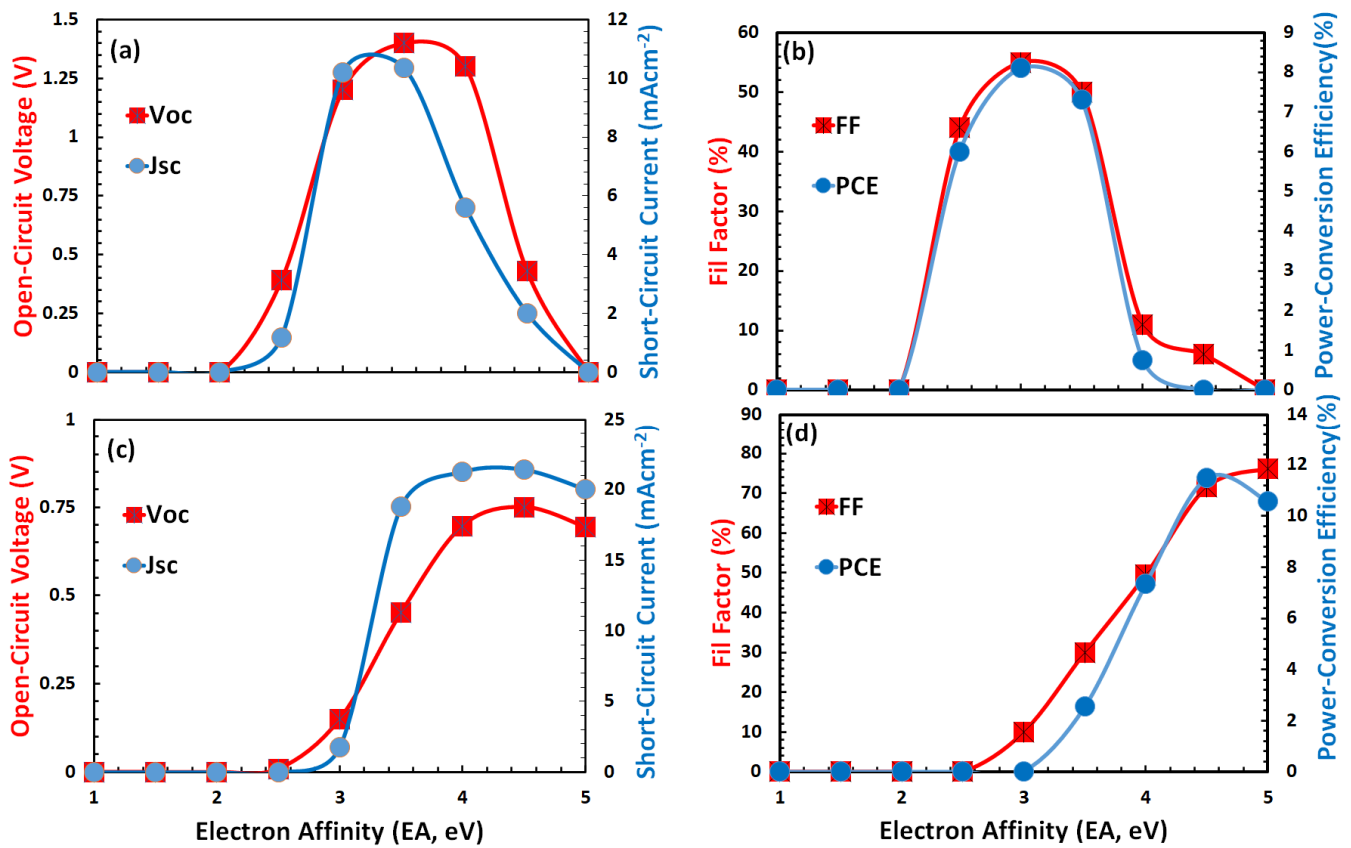


**Figure 3.** (a) Open-circuit voltage, short-circuit current, (b) fill factor, and power conversion efficiency of hole transport layer as a function of electron affinity. (c) Open-circuit voltage, short-circuit current, (d) fill factor, and power conversion efficiency of electron transport layer as a function of electron affinity for Cs<sub>2</sub>TiBr<sub>6</sub>-based solar cell.

### 3.2. Optimization of Energy Bandgap for Hole and Electron Transport Layer

In the second phase of the simulation, the optimized values of the energy bandgap for both hole and electron transport layers were explored. The energy bandgap of the charge transport layer fixes the HOMO level of both transport layers. For the hole transport layer, the higher HOMO level concerning the perovskite absorber helps the efficient extraction of the hole, and the lower LUMO level assists electron blocking from the absorber for perovskite solar cells and vice versa for the electron transport layer. From Table 2, it can be observed that the minimum, maximum, and median energy band gap values for the hole transport layer are 1.3, 3.8, and 2.98, respectively. Similarly, from Table 3, the minimum, maximum, and median energy band gap values for the electron transport layer are found as 1.9, 3.5, and 3.23, respectively. Thus, the optimized values of the energy bandgap are estimated within the practical range of 1 to 4 eV for both hole and electron transport layers. Therefore, the energy bandgap for the hole transport layer was calculated from the simulated photovoltaic response such as open-circuit voltage, short-circuit current, fill factor, and power conversion efficiency and the results are shown in Figure 4a,b, respectively. All these photovoltaic parameters show very similar responses. In the early stage, photovoltaic parameters and especially PCE is nearly zero up to 2 eV, and then PCE rises to reach a maximum of 3 eV of  $E_g$  and then starts to decrease. Similarly, Figure 4c,d show the simulated photovoltaic response of open-circuit voltage, short-circuit current, fill factor, and power conversion efficiency as a function of ETL energy bandgap ( $E_g$ ). All photovoltaic parameters increase as a function of energy bandgap, especially PCE, and become nearly saturated at 4 eV. Thus, it can be justified that the optimum values of the energy bandgap for the hole and electron transport layers are at 3.0 (PCE ~ 11.8%) and 4.0 eV (PCE ~ 12.8%), respectively.

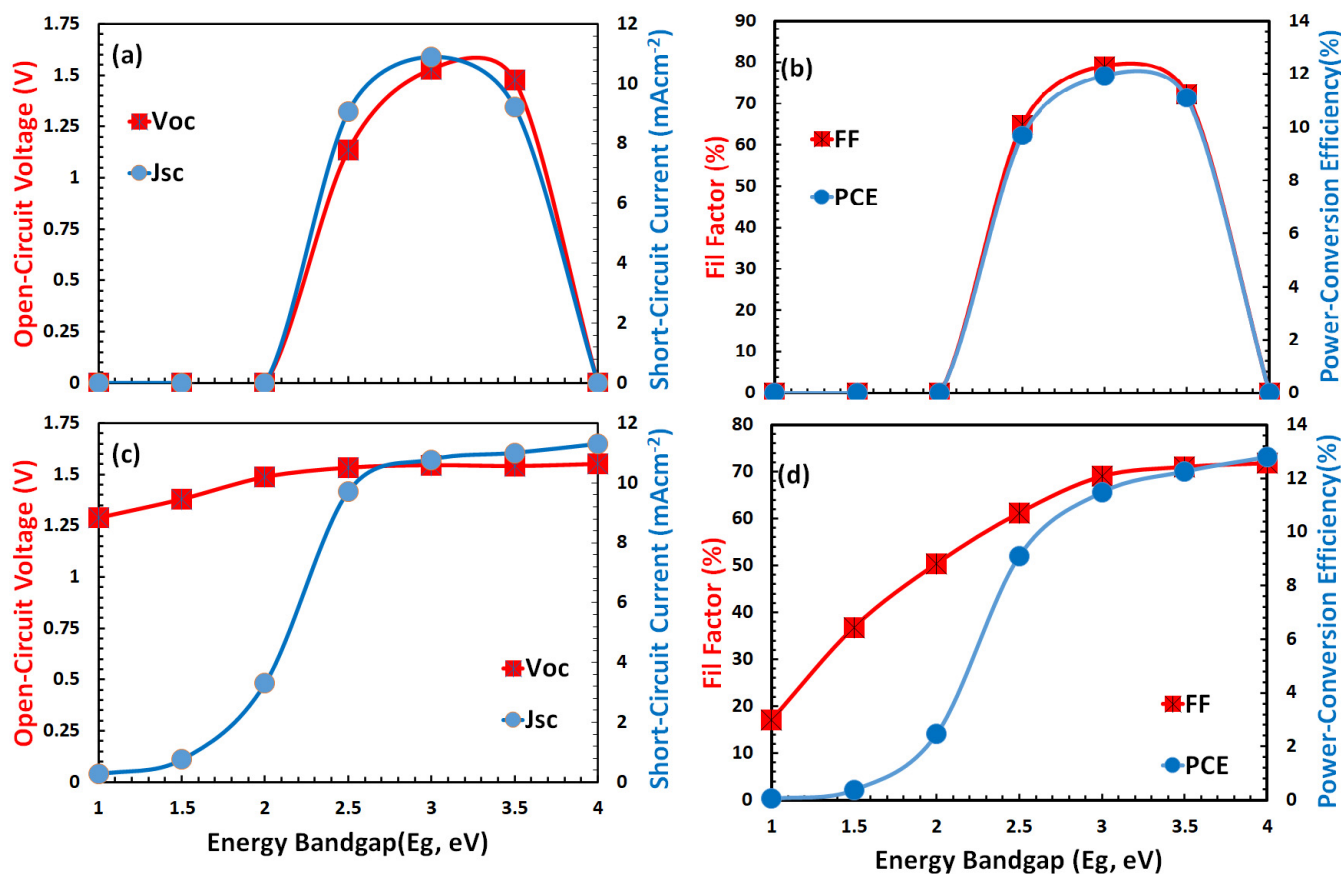
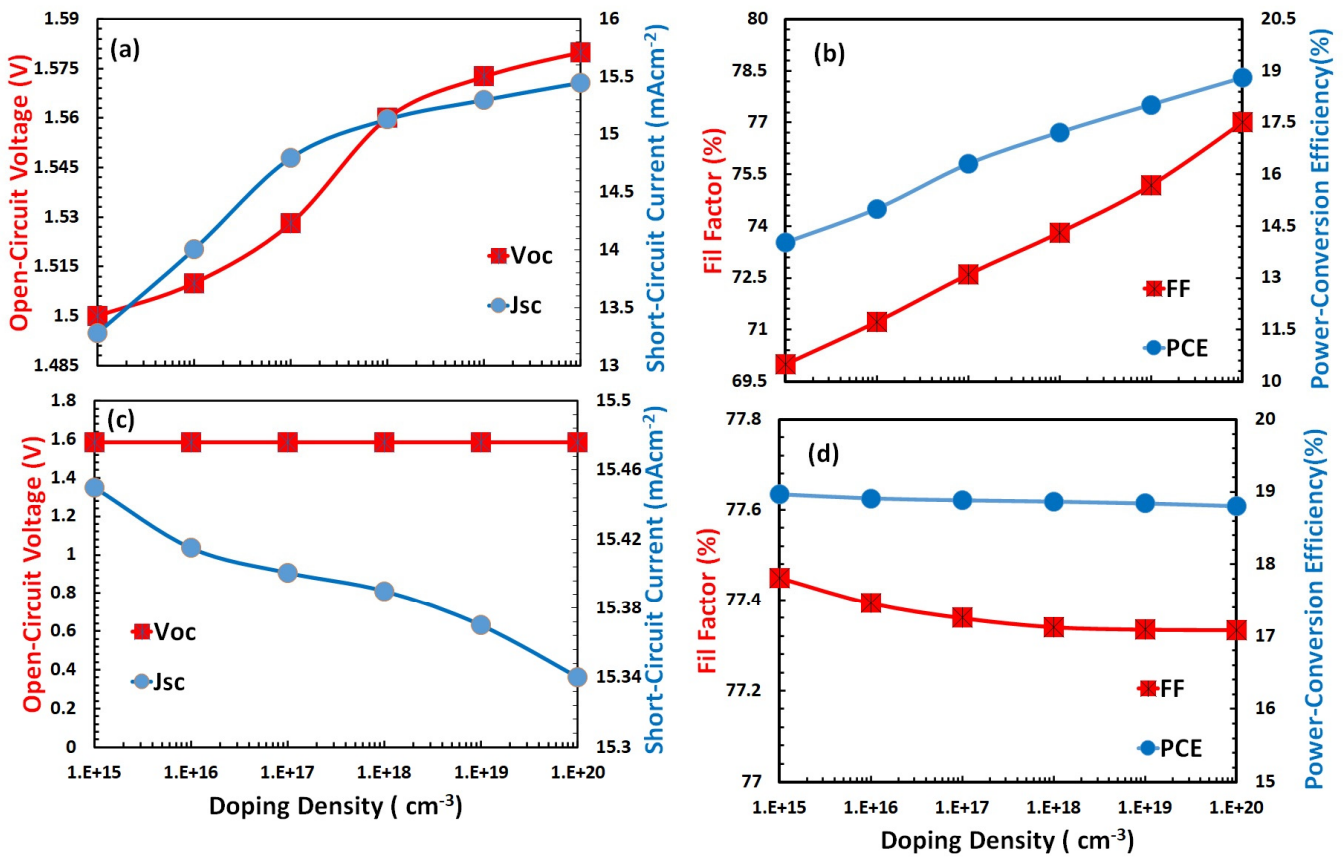


Figure 4. (a) Open-circuit voltage, short-circuit current, (b) fill factor, and power conversion efficiency of HTL as a function of electron affinity. (c) Open-circuit voltage, short-circuit current, (d) fill factor, and power conversion efficiency of ETL as a function of energy bandgap for Cs<sub>2</sub>TiBr<sub>6</sub>-based solar cell.

### 3.3. Optimization of Doping Density for Hole and Electron Transport Layer

In the third phase of the simulation, the acceptor/donor doping density ( $N_a/N_d$ ) of the hole/electron transport layer was optimized by incorporating the optimized electron affinity and energy bandgap of both transport layers. Generally, the charge transportation and collection process of the hole and electron transport layer improves by doping, and it may be due to the reduction in both layers' resistance for the formation of ohmic contacts to the respective electrodes [38–40]. It not only affects the charge transport and charge collection efficiency but also helps to manage the light-harvesting, and hence, it affects the overall device performance. At the same time, the doped hole and electron transport layers also cause an increase in the leakage current [41]; therefore, the doping optimization of both transport layers is very crucial for perovskite solar cells. Figure 5a,b shows the open-circuit voltage, short-circuit current, fill factor, and power conversion efficiency as a function of doping density of the hole transport layer, while Figure 5c,d show the open-circuit voltage, short-circuit current, fill factor, and power conversion efficiency as a function of doping density of the electron transport layer. The acceptor doping of the hole transport layer shows the increasing trend for all photovoltaic parameters, and especially PCE, and reaches the maximum (18.8%) at  $10^{20} \text{ cm}^{-3}$  for acceptor doping density. Correspondingly, donor doping of the electron transport layer shows a constant trend (approximately) for open-circuit voltage and PCE. Figure 5d shows that the PCE slightly increases and reaches a maximum (18.85%) at  $10^{16} \text{ cm}^{-3}$  and then follows a decreasing trend with a very low rate of PCE concerning donor doping density. Thus, it can be inferred from the above discussion that  $10^{20}/10^{16} \text{ cm}^{-3}$  is the most optimum doping density of the hole and electron transport layer, respectively, for Cs<sub>2</sub>TiBr<sub>6</sub>-based perovskite solar cells.



**Figure 5.** (a) Open-circuit voltage, short-circuit current, (b) fill factor, and power conversion efficiency of HTL as a function of electron affinity. (c) Open-circuit voltage, short-circuit current, (d) fill factor, and power conversion efficiency of ETL as a function of doping density for Cs<sub>2</sub>TiBr<sub>6</sub>-based solar cell.

### 3.4. Optimization of Thickness for Hole and Electron Transport Layer

In the second-to-last phase of the simulation, the thickness of the hole and electron transport layer was optimized for the Cs<sub>2</sub>TiBr<sub>6</sub> solar cell by incorporating the already optimized electron affinity, energy bandgap, and doping density for both transport layers. The thickness of the transport layer is another very important factor required to optimize for efficient Cs<sub>2</sub>TiBr<sub>6</sub>-based perovskite solar cells [42,43].

Thus, we first optimized the thickness of the hole (see Figure 6a,b) and then the electron transport layer (see Figure 6c,d) by using the optimized thickness of the hole transport layer. Figure 6a,b demonstrate that the open-circuit voltage, short-circuit current, fill factor, and power conversion efficiency increase as a function of hole transport layer thickness, but with different rates. The most important parameter PCE (see Figure 6b) increases (17.45%) up to a certain thickness (250 nm) and then becomes almost constant concerning HTL thickness. On the other hand, for the electron transport layer, the parameters such as open-circuit voltage, short-circuit current, fill factor, and power conversion efficiency linearly decreases as a function of a thickness (Figure 6c,d) and gives the maximum PCE (20.4%) at 25 nm. This thickness may be the result of the interplay optimization between the higher optical transmittance, efficient electron charge transport, and low leakage current with a small recombination rate for Cs<sub>2</sub>TiBr<sub>6</sub>-based perovskite solar cells.

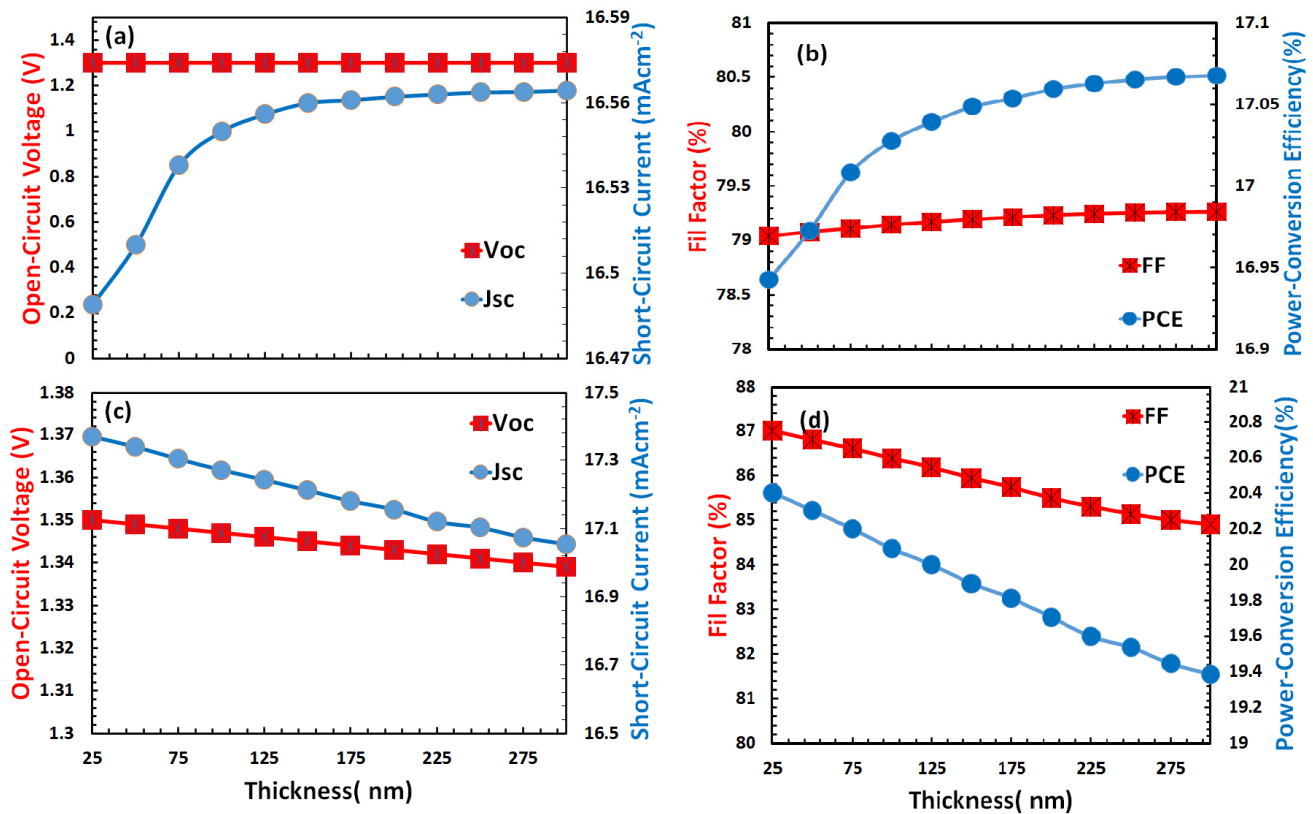


**Figure 6.** (a) Open-circuit voltage, short-circuit current, (b) fill factor, and power conversion efficiency of HTL as a function of electron affinity. (c) Open-circuit voltage, short-circuit current, (d) fill factor, and power conversion efficiency of ETL as a function of film thickness for Cs<sub>2</sub>TiBr<sub>6</sub>-based solar cell.

### 3.5. Device Energy Level and Electric Field Distribution of ETL/Cs<sub>2</sub>TiBr<sub>6</sub>/HTL

Figure 7 shows the electronic energy level diagram for the optimized ETL/Cs<sub>2</sub>TiBr<sub>6</sub>/HTL solar cell. The figure depicts that the HOMO (−6.0 eV) and LUMO (−3.0 eV) level of the hole transport layer support the efficient injection of the hole and blocking of an electron concerning the Cs<sub>2</sub>TiBr<sub>6</sub> absorber layer. Similarly, the HOMO (−8.6 eV) and LUMO (−4.6 eV) level of the electron transport layer helps the efficient injection of electrons and blocking of the hole concerning the Cs<sub>2</sub>TiBr<sub>6</sub> absorber layer. Therefore, the energy level alignment of the hole and electron transport layer with the Cs<sub>2</sub>TiBr<sub>6</sub> perovskite absorber offers the basic electronic structure framework for highly efficient ETL/Cs<sub>2</sub>TiBr<sub>6</sub>/HTL-based perovskite solar cells.

The electric field distribution inside an electronic structure of a perovskite solar cell plays a very crucial role to define the overall carrier transport, recombination, and, hence, PCE of the perovskite solar cell. It is a direct function of the electrical nature of materials (HTL, ETL, and perovskite), doping density, band alignment, and interface parameters.

In our case, both HTL (10<sup>20</sup> cm<sup>−3</sup>) and ETL (10<sup>16</sup> cm<sup>−3</sup>) are unequally doped, while the thickness of the HTL (250 nm) is much larger than that of the ETL (25 nm). Therefore, an asymmetric electric field profile at HTL/Cs<sub>2</sub>TiBr<sub>6</sub> and Cs<sub>2</sub>TiBr<sub>6</sub>/ETL is observed, as shown in Figure 8, which is responsible for the high open-circuit voltage and, hence, PCE. Thus, when photons fall on the Cs<sub>2</sub>TiBr<sub>6</sub> layer, they are optically absorbed, and many excitons are generated with low binding energy, as well as high diffusion length. When these excitons reach their respective interfaces, they are dissociated into the free carrier due to the high interface electric field and are passed to either the HTL or ETL depending on the nature of the free carrier.

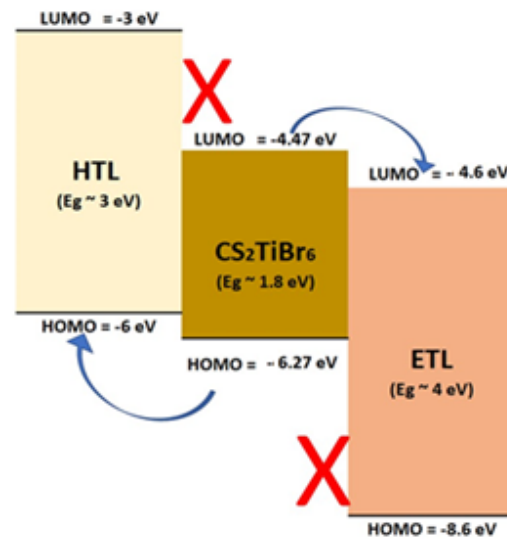


Figure 7. Energy level alignment for Cs<sub>2</sub>TiBr<sub>6</sub> cell with highly suitable band structure of hole transport and electron transport layer for an efficient photovoltaic response.

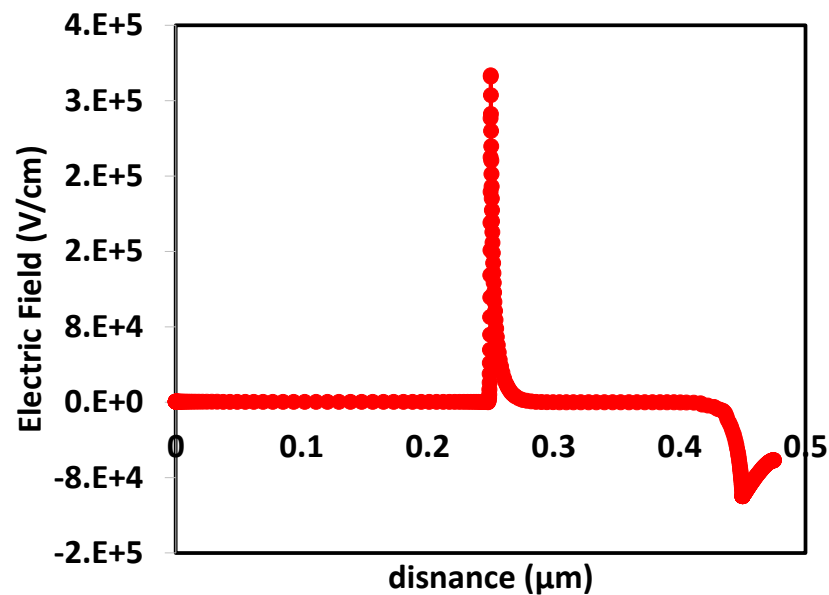


Figure 8. Electric field distribution inside ETL (25 nm)/Cs<sub>2</sub>TiBr<sub>6</sub> (200 nm)/HTL (250 nm) solar cell.

### 3.6. Selection of Hole and Electron Transport Layer

From the above discussion, it can be concluded that the proper selection of the hole transport layer with these physical parameters (electron affinity =  $-3$  eV, energy band gap =  $3$  eV,  $N_a = 10^{20}$  cm<sup>-3</sup>, and thickness =  $250$  nm), as well as the use of an appropriate electron transport layer with physical parameters (electron affinity =  $-4.6$  eV, energy band gap =  $4$  eV,  $N_d = 10^{16}$  cm<sup>-3</sup>, and thickness =  $25$  nm), can give a maximum PCE up to  $20.41\%$  for the Cs<sub>2</sub>TiBr<sub>6</sub>-based perovskite solar cell. Unfortunately, not a single hole transport layer and electron transport layer material were available, as shown in Tables 2 and 3, respectively, having a similar energy bandgap and electron affinity to fulfill the requirements for maximum PCE. Just for practical purposes, NPB as a hole transport layer material and CeO<sub>x</sub> as an electron transport layer materials were selected as their energy bandgap, and the activation energy is very close compared to the other materials listed in Tables 2 and 3, respectively. Although SnO<sub>2</sub> has a good electronic structure and shows more efficient performance as an ETL, the major issue with SnO<sub>2</sub> as the ETL is that it offers some limitations for thin-film deposition and deteriorates at high temperatures

during fabrication processes [44]. Therefore, we selected cerium oxide ( $\text{CeO}_x$ ) as the best ETL from Table 3.  $\text{CeO}_x$  as an ETL has a very similar electronic structure compared to  $\text{SnO}_2$ . It is a wide-bandgap semiconductor that has high conductivity, chemical and thermal stability, transparency in the visible range, and a good dielectric constant [28]. The physical parameters for NPB and  $\text{CeO}_x$  were taken from the published results and are displayed in Table 5 [15,45,46]. The photovoltaic response of the proposed device as  $\text{CeO}_x/\text{Cs}_2\text{TiBr}_6/\text{NPB}$  was simulated and compared with the photovoltaic response of an ideal ETL/ $\text{Cs}_2\text{TiBr}_6/\text{HTL}$  solar cell, and the output results are shown in Figure 9. The figure shows that the proposed solar cell performs well, and its PCE is  $\sim 17.9\%$ , which is less than that of the ideal (PCE is  $20.4\%$ ) solar cell. The simulated photovoltaic parameters such as open-circuit voltage, short circuit current, fill factor, and PCE of both solar cells are tabulated in the inset of Figure 9. The inset table depicts that the open-circuit voltage and fill factor of the proposed solar cell are nearly the same as those of the ideal one. The short-circuit current is the main parameter that causes a lowering of the PCE of the proposed solar cell compared to the ideal solar cell. The short-circuit current is directly dependent on the electronic structure of both transport layers [47]; therefore, it is highly recommended to tailor the electronic structure of both transport layers according to the simulation results for the highly efficient photovoltaic response. Different strategies are being reported in the literature to fabricate the hole transport and electron transport layers for the required electronic structure for efficient solar cells. Broadly speaking, these strategies can be classified into the following types: (i) chemical tailoring [48], (ii) solvent treatment [49], and (iii) using an interface buffer layer [50,51]. Anyone or a combination of these techniques can be applied successfully for the fabrication of hole and electron transport layers for efficient  $\text{Cs}_2\text{TiBr}_6$ -based perovskite solar cells.

**Table 5.** Physical parameters of  $\text{Cs}_2\text{TiBr}_6$  and NPB (HTL) and  $\text{CeO}_x$  (ETL) were used in the simulation. Both NPB and  $\text{CeO}_x$  are selected based on the closeness of the energy bandgap and electron affinity with the simulation results.

Physical Parameters	Symbol	Unit	NPB (HTL)	$\text{Cs}_2\text{TiBr}_6$	$\text{CeO}_x$ (ETL)
Thickness	Th	nm	250	150	25
Energy Band Gap	$E_g$	eV	2.4	1.8	3.5
Electron Affinity	$\chi$	eV	3	4.47	4.4
Dielectric Permittivity (Relative)	$\epsilon$	-	3	10	9
Effective Density of States at Valence Band	$N_V$	$\text{cm}^{-3}$	$1 \times 10^{21}$	$6 \times 10^{19}$	$1 \times 10^{20}$
Effective Density of States at Conduction Band	$N_C$	$\text{cm}^{-3}$	$1 \times 10^{21}$	$2 \times 10^{19}$	$2 \times 10^{21}$
Hole Thermal Velocity	$V_e$	cm/s	$1 \times 10^7$	$1 \times 10^7$	$1 \times 10^7$
electron Thermal Velocity	$V_h$	cm/s	$1 \times 10^7$	$1 \times 10^7$	$1 \times 10^7$
Electron Mobility	$\mu_e$	$\text{cm}^2/\text{V.s}$	$6 \times 10^{-6}$	4.4	100
Hole Mobility	$\mu_h$	$\text{cm}^2/\text{V.s}$	$6.1 \times 10^{-4}$	2.5	25
Uniform Shallow Donor Doping	$N_d$	$\text{cm}^{-3}$	0	$1 \times 10^{17}$	$1 \times 10^{16}$
Uniform Shallow Acceptor Doping	$N_a$	$\text{cm}^{-3}$	$1 \times 10^{20}$	$1 \times 10^{17}$	0
Defect Density	$N_t$	$\text{cm}^{-3}$	$1 \times 10^{14}$	$1 \times 10^{15}$	$1 \times 10^{15}$
References			[15,45]	[9,10,13,14]	[46]

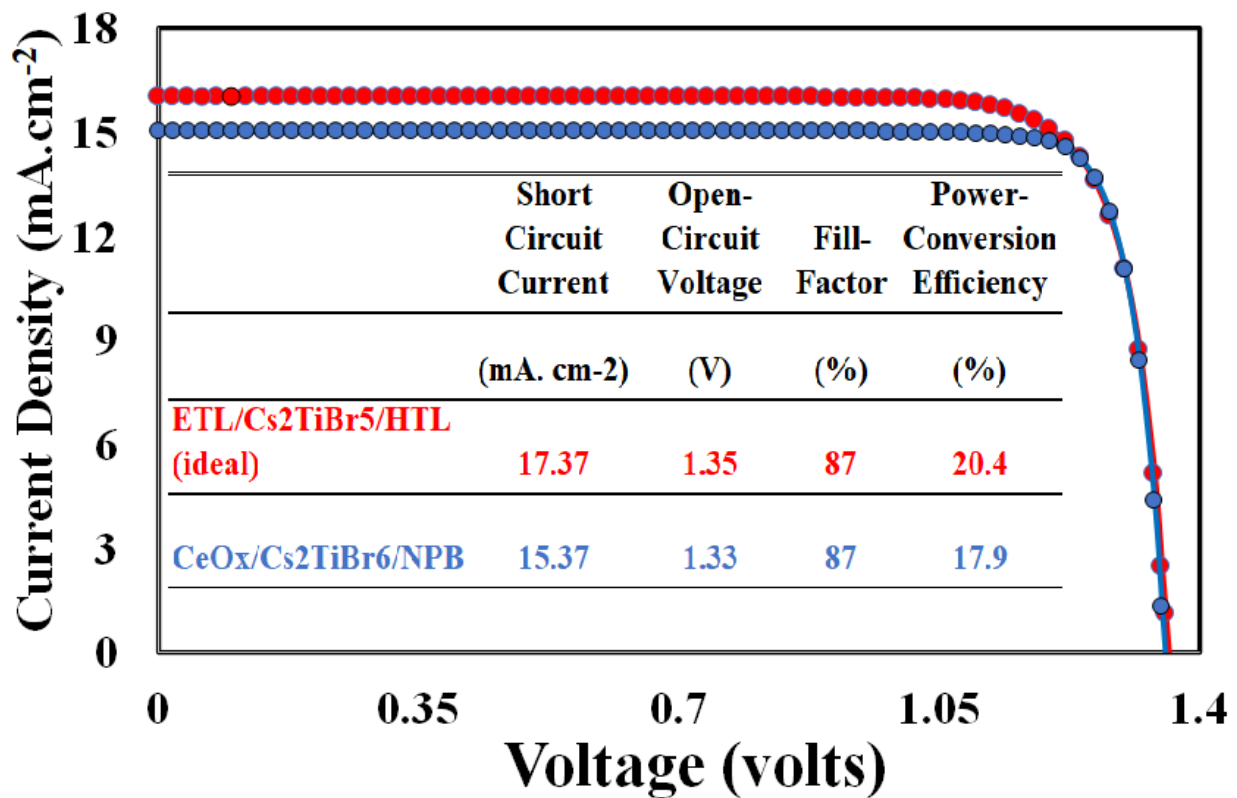


**Figure 9.** Photo current-voltage response of ETL/Cs<sub>2</sub>TiBr<sub>6</sub>/HTL and CeO<sub>x</sub>/Cs<sub>2</sub>TiBr<sub>6</sub>/NPB solar cells. The inset lists the photovoltaic parameters such as short-circuit current, open-circuit voltage, fill factor, and PCE for both solar cells.

#### 4. Conclusions

Due to the toxic nature of methylammonium lead halide, many other lead-free perovskite materials have been heavily investigated and reported for photovoltaic applications. Among these, cesium-titanium (IV) bromide (Cs<sub>2</sub>TiBr<sub>6</sub>) is considered one of the best alternatives, but it still faces a lack of higher PCE due to the unavailability of the matched hole and electron transport layers. Therefore, for the highly efficient photovoltaic response, the physical parameters such as electron affinity, energy bandgap, doping density, and film thickness of ideal hole and electron transport layers were determined for the Cs<sub>2</sub>TiBr<sub>6</sub>-based solar cell through SCAPS-1D simulation. It was observed that the proper hole transport layer (electron affinity = −3 eV, energy band gap = 3 eV, N<sub>a</sub> = 10<sup>20</sup> cm<sup>−3</sup>, and thickness = 250 nm), as well as using the appropriate electron transport layer (electron affinity = −4.6 eV, energy band gap = 4 eV, N<sub>d</sub> = 10<sup>16</sup> cm<sup>−3</sup>, and thickness = 25 nm), can give a maximum PCE up to 20.41% for Cs<sub>2</sub>TiBr<sub>6</sub>-based perovskite solar cells. Unfortunately, not a single hole and electron transport material with the required electronic structure was found. However, NPB and CeO<sub>x</sub> were selected as hole and electron transport layers, respectively, based on the closed electronic structure compared to the simulation results, and the simulated maximum PCE was found as ~17.9% for the CeO<sub>x</sub>/Cs<sub>2</sub>TiBr<sub>6</sub>/NPB solar cell. We believe that the outcome of this study will help the development and fabrication of highly efficient lead-free perovskite solar cells.

**Funding:** Deputyship for Research & Innovation, Ministry of education in Saudi Arabia for funding this research work through project number 20-UQ-IF-P2-001.

**Acknowledgments:** The author extends their appreciation to the Deputyship for Research & innovation, Ministry of education in Saudi Arabia for funding this research work through the project number 20-UQU-IF-P2-001.

**Conflicts of Interest:** The author declares that there are no conflict of interest to report regarding the pre-sent study.

## References

1. Kabir, E.; Kumar, P.; Kumar, S.; Adelodun, A.A.; Kim, K.-H. Solar energy: Potential and future prospects. *Renew. Sustain. Energy Rev.* **2018**, *82*, 894–900. [[CrossRef](#)]
2. Nazeeruddin, M.K. Twenty-five years of low-cost solar cells. *Nature* **2016**, *538*, 463–464. [[CrossRef](#)] [[PubMed](#)]
3. Karimov, K.S.; Ahmed, M.; Moiz, S.; Fedorov, M. Temperature-dependent properties of organic-on-inorganic Ag/p-CuPc/n-GaAs/Ag photoelectric cell. *Sol. Energy Mater. Sol. Cells* **2005**, *87*, 61–75. [[CrossRef](#)]
4. Green, M.A. The path to 25% silicon solar cell efficiency: History of silicon cell evolution. *Prog. Photovolt. Res. Appl.* **2009**, *17*, 183–189. [[CrossRef](#)]
5. Pizzini, S. Towards solar grade silicon: Challenges and benefits for low cost photovoltaics. *Sol. Energy Mater. Sol. Cells* **2010**, *94*, 1528–1533. [[CrossRef](#)]
6. Kim, G.-H.; Kim, D.S. Development of perovskite solar cells with >25% conversion efficiency. *Joule* **2021**, *5*, 1033–1035. [[CrossRef](#)]
7. Babayigit, A.; Ethirajan, A.; Muller, M.; Conings, B. Toxicity of organometal halide perovskite solar cells. *Nat. Mater.* **2016**, *15*, 247–251. [[CrossRef](#)]
8. Giustino, F.; Snaith, H.J. Toward Lead-Free Perovskite Solar Cells. *ACS Energy Lett.* **2016**, *1*, 1233–1240. [[CrossRef](#)]
9. Chen, M.; Ju, M.-G.; Carl, A.; Zong, Y.; Grimm, R.L.; Gu, J.; Zeng, X.C.; Zhou, Y.; Padture, N.P. Cesium Titanium(IV) Bromide Thin Films Based Stable Lead-free Perovskite Solar Cells. *Joule* **2018**, *2*, 558–570. [[CrossRef](#)]
10. Ju, M.-G.; Chen, M.; Zhou, Y.; Garces, H.F.; Dai, J.; Ma, L.; Padture, N.P.; Zeng, X.C. Earth-Abundant Nontoxic Titanium(IV)-based Vacancy-Ordered Double Perovskite Halides with Tunable 1.0 to 1.8 eV Bandgaps for Photovoltaic Applications. *ACS Energy Lett.* **2018**, *3*, 297–304. [[CrossRef](#)]
11. Pecunia, V.; Occhipinti, L.G.; Chakraborty, A.; Pan, Y.; Peng, Y. Lead-free halide perovskite photovoltaics: Challenges, open questions, and opportunities. *APL Mater.* **2020**, *8*, 100901. [[CrossRef](#)]
12. Grandhi, G.; Matuhina, A.; Liu, M.; Annurakshita, S.; Ali-Löytty, H.; Bautista, G.; Vivo, P. Lead-Free Cesium Titanium Bromide Double Perovskite Nanocrystals. *Nanomaterials* **2021**, *11*, 1458. [[CrossRef](#)]
13. Chakraborty, K.; Choudhury, M.G.; Paul, S. Numerical study of Cs<sub>2</sub>TiX<sub>6</sub> (X = Br<sup>-</sup>, I<sup>-</sup>, F<sup>-</sup> and Cl<sup>-</sup>) based perovskite solar cell using SCAPS-1D device simulation. *Sol. Energy* **2019**, *194*, 886–892. [[CrossRef](#)]
14. Jani, R.; Islam, T.; Al Amin, S.M.; Sami, S.U.; Shorowordi, K.M.; Hossain, M.I.; Chowdhury, S.; Nishat, S.S.; Ahmed, S. Exploring solar cell performance of inorganic Cs<sub>2</sub>TiBr<sub>6</sub> halide double perovskite: A numerical study. *Superlattices Microstruct.* **2020**, *146*, 106652. [[CrossRef](#)]
15. Moiz, S.; Alahmadi, A. Design of Dopant and Lead-Free Novel Perovskite Solar Cell for 16.85% Efficiency. *Polymers* **2021**, *13*, 2110. [[CrossRef](#)] [[PubMed](#)]
16. Moiz, S.A.; Alahmadi, A.N.M.; Aljohani, A.J. Design of a Novel Lead-Free Perovskite Solar Cell for 17.83% Efficiency. *IEEE Access* **2021**, *9*, 54254–54263. [[CrossRef](#)]
17. Qiao, L.; Fang, W.-H.; Long, R. Dopant Control of Electron–Hole Recombination in Cesium–Titanium Halide Double Perovskite by Time Domain Ab Initio Simulation: Codoping Supersedes Monodoping. *J. Phys. Chem. Lett.* **2018**, *9*, 6907–6914. [[CrossRef](#)] [[PubMed](#)]
18. Park, S.M.; Mazza, S.M.; Liang, Z.; Abtahi, A.; Boehm, A.M.; Parkin, S.R.; Anthony, J.E.; Graham, K.R. Processing Dependent Influence of the Hole Transport Layer Ionization Energy on Methylammonium Lead Iodide Perovskite Photovoltaics. *ACS Appl. Mater. Interfaces* **2018**, *10*, 15548–15557. [[CrossRef](#)] [[PubMed](#)]
19. Lopez-Varo, P.; Jiménez-Tejada, J.A.; García-Rosell, M.; Ravishankar, S.; Garcia-Belmonte, G.; Bisquert, J.; Almora, O. Device Physics of Hybrid Perovskite Solar cells: Theory and Experiment. *Adv. Energy Mater.* **2018**, *8*, 1702772. [[CrossRef](#)]
20. Yin, W.-J.; Shi, T.; Yan, Y. Unusual defect physics in CH<sub>3</sub>NH<sub>3</sub>PbI<sub>3</sub> perovskite solar cell absorber. *Appl. Phys. Lett.* **2014**, *104*, 063903. [[CrossRef](#)]
21. Moiz, S.A.; Alahmadi, A.N.M.; Aljohani, A.J. Design of Silicon Nanowire Array for PEDOT:PSS-Silicon Nanowire-Based Hybrid Solar Cell. *Energies* **2020**, *13*, 3797. [[CrossRef](#)]
22. Moiz, S.A.; Nahhas, A.; Um, H.-D.; Jee, S.-W.; Cho, H.K.; Kim, S.-W.; Lee, J.-H. A stamped PEDOT:PSS–silicon nanowire hybrid solar cell. *Nanotechnology* **2012**, *23*, 145401. [[CrossRef](#)]
23. Verschraegen, J.; Burgelman, M. Numerical modeling of intra-band tunneling for heterojunction solar cells in scaps. *Thin Solid Films* **2007**, *515*, 6276–6279. [[CrossRef](#)]
24. Burgelman, M.; Verschraegen, J.; Degraeve, S.; Nollet, P. Modeling thin-film PV devices. *Prog. Photovolt. Res. Appl.* **2004**, *12*, 143–153. [[CrossRef](#)]
25. Xiao, Z.; Yuan, Y.; Wang, Q.; Shao, Y.; Bai, Y.; Deng, Y.; Dong, Q.; Hu, M.; Bi, C.; Huang, J. Thin-film semiconductor perspective of organometal trihalide perovskite materials for high-efficiency solar cells. *Mater. Sci. Eng. R Rep.* **2016**, *101*, 1–38. [[CrossRef](#)]
26. Burgelman, M.; Decock, K.; Khelifi, S.; Abass, A. Advanced electrical simulation of thin film solar cells. *Thin Solid Films* **2013**, *535*, 296–301. [[CrossRef](#)]
27. Liu, T.; Chen, K.; Hu, Q.; Zhu, R.; Gong, Q. Inverted Perovskite Solar Cells: Progresses and Perspectives. *Adv. Energy Mater.* **2016**, *6*, 1600457. [[CrossRef](#)]

28. Wang, X.; Deng, L.-L.; Wang, L.-Y.; Dai, S.-M.; Xing, Z.; Zhan, X.-X.; Lu, X.-Z.; Xie, S.-Y.; Huang, R.-B.; Zheng, L.-S. Cerium oxide standing out as an electron transport layer for efficient and stable perovskite solar cells processed at low temperature. *J. Mater. Chem. A* **2016**, *5*, 1706–1712. [[CrossRef](#)]
29. Azri, F.; Meftah, A.; Sengouga, N.; Meftah, A. Electron and hole transport layers optimization by numerical simulation of a perovskite solar cell. *Sol. Energy* **2019**, *181*, 372–378. [[CrossRef](#)]
30. Lin, P.; Lin, L.; Yu, J.; Cheng, S.; Lu, P.; Zheng, Q. Numerical Simulation of Cu<sub>2</sub>ZnSnS<sub>4</sub> Based Solar Cells with In<sub>2</sub>S<sub>3</sub> Buffer Layers by SCAPS-1D. *J. Appl. Sci. Eng.* **2014**, *17*, 383–390. [[CrossRef](#)]
31. Ahmed, S.; Jannat, F.; Khan, A.K.; Alim, M.A. Numerical development of eco-friendly Cs<sub>2</sub>TiBr<sub>6</sub> based perovskite solar cell with all-inorganic charge transport materials via SCAPS-1D. *Optik* **2020**, *225*, 165765. [[CrossRef](#)]
32. Lam, N.D.; Nguyen, D.L. Modelling and numerical analysis of ZnO/CuO/Cu<sub>2</sub>O heterojunction solar cell using SCAPS. *Eng. Res. Express* **2020**, *2*, 025033. [[CrossRef](#)]
33. Hima, A.; Lakhdar, N. Enhancement of efficiency and stability of CH<sub>3</sub>NH<sub>3</sub>GeI<sub>3</sub> solar cells with CuSbS<sub>2</sub>. *Opt. Mater.* **2019**, *99*, 109607. [[CrossRef](#)]
34. Jayan, K.D. Enhancement of efficiency of (FA)<sub>2</sub>BiCuI<sub>6</sub> based perovskite solar cells with inorganic transport layers. *Opt. Mater.* **2021**, *122*, 111671. [[CrossRef](#)]
35. Karthick, S.; Bouclé, J.; Velumani, S. Effect of bismuth iodide (BiI<sub>3</sub>) interfacial layer with different HTL's in FAPI based perovskite solar cell—SCAPS—1D study. *Sol. Energy* **2021**, *218*, 157–168. [[CrossRef](#)]
36. Pham, D.P.; Lee, S.; Kim, Y.; Yi, J. Band-offset reduction for effective hole carrier collection in bifacial silicon heterojunction solar cells. *J. Phys. Chem. Solids* **2021**, *154*, 110059. [[CrossRef](#)]
37. Um, H.-D.; Moiz, S.A.; Park, K.-T.; Jung, J.-Y.; Jee, S.-W.; Ahn, C.H.; Kim, D.-W.; Cho, H.K.; Lee, J.-H. Highly selective spectral response with enhanced responsivity of n-ZnO/p-Si radial heterojunction nanowire photodiodes. *Appl. Phys. Lett.* **2011**, *98*, 033102. [[CrossRef](#)]
38. Subair, R.; Di Girolamo, D.; Bodik, M.; Nadazdy, V.; Li, B.; Nadazdy, P.; Markovic, Z.; Benkovicova, M.; Chlpik, J.; Kotlar, M.; et al. Effect of the doping of PC61BM electron transport layer with carbon nanodots on the performance of inverted planar MAPbI<sub>3</sub> perovskite solar cells. *Sol. Energy* **2019**, *189*, 426–434. [[CrossRef](#)]
39. Gotanda, T.; Kimata, H.; Xue, D.; Asai, H.; Shimazaki, A.; Wakamiya, A.; Marumoto, K. Direct observation of charge transfer at the interface between PEDOT:PSS and perovskite layers. *Appl. Phys. Express* **2019**, *12*, 041002. [[CrossRef](#)]
40. Moiz, S.A.; Khan, I.A.; Younis, W.A.; Masud, M.I.; Ismail, Y.; Khawaja, Y.M. Solvent induced charge transport mechanism for conducting polymer at higher temperature. *Mater. Res. Express* **2020**, *7*, 095304. [[CrossRef](#)]
41. Schloemer, T.H.; Christians, J.A.; Luther, J.M.; Sellinger, A. Doping strategies for small molecule organic hole-transport materials: Impacts on perovskite solar cell performance and stability. *Chem. Sci.* **2019**, *10*, 1904–1935. [[CrossRef](#)] [[PubMed](#)]
42. Marinova, N.; Tress, W.; Humphry-Baker, R.; Dar, M.I.; Bojinov, V.; Zakeeruddin, S.M.; Nazeeruddin, M.K.; Grätzel, M. Light Harvesting and Charge Recombination in CH<sub>3</sub>NH<sub>3</sub>PbI<sub>3</sub> Perovskite Solar Cells Studied by Hole Transport Layer Thickness Variation. *ACS Nano* **2015**, *9*, 4200–4209. [[CrossRef](#)] [[PubMed](#)]
43. Kim, G.-W.; Shinde, D.V.; Park, T. Thickness of the hole transport layer in perovskite solar cells: Performance versus reproducibility. *RSC Adv.* **2015**, *5*, 99356–99360. [[CrossRef](#)]
44. Xiong, L.; Guo, Y.; Wen, J.; Liu, H.; Yang, G.; Qin, P.; Fang, G. Review on the Application of SnO<sub>2</sub> in Perovskite Solar Cells. *Adv. Funct. Mater.* **2018**, *28*, 1802757. [[CrossRef](#)]
45. Karimi, E.; Ghorashi, S. Investigation of the influence of different hole-transporting materials on the performance of perovskite solar cells. *Optik* **2017**, *130*, 650–658. [[CrossRef](#)]
46. Ahmmed, S.; Karim, A.; Rahman, H.; Aktar, A.; Islam, R.; Islam, A.; Ismail, A.B.M. Performance analysis of lead-free CsBi<sub>3</sub>I<sub>10</sub>-based perovskite solar cell through the numerical calculation. *Sol. Energy* **2021**, *226*, 54–63. [[CrossRef](#)]
47. Wu, M.-C.; Chan, S.-H.; Jao, M.-H.; Su, W.-F. Enhanced short-circuit current density of perovskite solar cells using Zn-doped TiO<sub>2</sub> as electron transport layer. *Sol. Energy Mater. Sol. Cells* **2016**, *157*, 447–453. [[CrossRef](#)]
48. Schulz, P.; Kelly, L.L.; Winget, P.; Li, H.; Kim, H.; Ndione, P.F.; Sigdel, A.K.; Berry, J.J.; Graham, S.; Brédas, J.-L.; et al. Tailoring Electron-Transfer Barriers for Zinc Oxide/C<sub>60</sub>Fullerene Interfaces. *Adv. Funct. Mater.* **2014**, *24*, 7381–7389. [[CrossRef](#)]
49. Park, Y.I.; Kuo, C.-Y.; Martinez, J.S.; Park, Y.-S.; Postupna, O.; Zhugayevych, A.; Kim, S.; Park, J.; Tretiak, S.; Wang, H.-L. Tailored Electronic Structure and Optical Properties of Conjugated Systems through Aggregates and Dipole–Dipole Interactions. *ACS Appl. Mater. Interfaces* **2013**, *5*, 4685–4695. [[CrossRef](#)]
50. Moiz, S.; Alahmadi, A.; Karimov, K. Improved organic solar cell by incorporating silver nanoparticles embedded polyaniline as buffer layer. *Solid-State Electron.* **2019**, *163*, 107658. [[CrossRef](#)]
51. Zheng, Z.; Wang, R.; Yao, H.; Xie, S.; Zhang, Y.; Hou, J.; Zhou, H.; Tang, Z. Polyamino acid interlayer facilitates electron extraction in narrow band gap fullerene-free organic solar cells with an outstanding short-circuit current. *Nano Energy* **2018**, *50*, 169–175. [[CrossRef](#)]